Cation/anion-doping induced electronic structure regulation strategy to boost the catalytic hydrogen evolution from ammonia borane hydrolysis

Chongyang Yuan [a], Tian Xu [a], Miao Guo [a], Tengfei Zhang [b], Xuebin Yu [a,*]

[a] Department of Materials Science, Fudan University, Shanghai 200433, China
[b] Centre for Hydrogenergy, College of Materials Science and Technology, Nanjing University of Aeronautics and Astronautics, Nanjing, Jiangsu 210016, China

A R T I C L E   I N F O

A B S T R A C T

Exploration of high-performance and cost-effective catalysts for hydrogen production from chemical hydrogen-storage materials is vital but still a challenge. Herein we report the synthesis of a ZIF-67 derived Co_3O_4 nanoparticles in a carbon-based nanoframeworks and discover that doping phosphorus into Co_3O_4 has a unique electronic structure modulation effect, resulting in a nearly 29-fold enhancement of the catalytic activity for ammonia borane hydrolytic dehydrogenation. Furthermore, combining the P doping with Cu doping, a strong synergistic effect is realized to boost the catalytic H_2 generation with an astonishing nearly 51-fold improvement (turnover frequency, TOF = 35.6 min^{-1}). Based on the experimental and theoretical results, the enhanced performance is attributed to the optimization of the electronic configuration and the downshift of d-band center over Co_3O_4 after P/Cu doping, thereby facilitating H_2O dissociation and hydrogen desorption. This work will be applicable to designing other metal based nanocatalysts toward more efficient energy conversion reactions.

1. Introduction

Hydrogen as a new popular clearly energy with many advantages like high energy density, rich source and no pollution has attracted more and more focus from researchers worldwide. Hydrogen energy has been widely recognized as a clean efficient and renewable energy [1,2]. Since hydrogen has the characteristics of low density and wide explosion limit, how to store and transport hydrogen efficiently and conveniently has become a bottleneck restricting the development and utilization of hydrogen energy [2–4]. The development of an efficient hydrogen storage material is currently one of the hot topics in the field of hydrogen energy research. Chemical storage of hydrogen has been considered as an effective way for the storage of hydrogen, but the controlled release of hydrogen from the chemical storage materials is still a challenge [5–7]. As one of common chemical hydrogen storage materials, ammonia borane (NH_3BH_3, later shortened to AB), with the advantages of high hydrogen desorption density (19.6 wt%), mild hydrogen generation condition, high stability in both water solution and air, and non-toxicity, has been extensively studied [8–11]. AB can release hydrogen through pyrolysis [12,13], hydrolysis [5,14], alcoholysis [15, 16], etc. The AB hydrolysis reaction is as follows:

$$NH_3BH_3 + 2H_2O \xrightarrow{\text{catalyst}} NH_4BO_2 + 3H_2 \qquad (1)$$
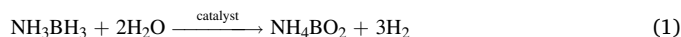
The way of AB hydrolysis has been expected to produce dihydrogen controllably by using suitable catalysts from the Eq. (1). In recent years, various catalysts, in the catalysis of AB hydrolysis, involving metals [17, 18], oxides [19,20], phosphides [21,22] and other catalysts [23–25] have been developed. Among these different catalysts, the noble-metal based catalysts (such as Pt, Rh, Ru, and Pd) tend to exhibit better catalytic performance [26–28]. Nevertheless, the problem of the noble metal catalysts that we must consider is their high cost in the actual application of AB hydrolysis. Therefore, researchers have turned their eyes to the transitional metal-based catalysts [29–32], and further discovered many modification approaches to improve the catalytic activity of transitional metal-based catalysts such as size control [33], crystal facet adjustment [34,35], component and architecture regulation [30,36], etc. Despite the impressive research progress, non-noble transition metal-based catalysts still show limited performance in catalyzing AB hydrolytic dehydrogenation, not as well as well-recognized noble metals. Accordingly, developing promising strategy to further promote catalytic performance of transition metal-based catalysts remain a massive challenge for AB hydrolytic dehydrogenation.

Lately, ion doping has emerged as a robust protocol to tailor the crystal structure and chemical properties of the nanomaterials.

---

* Corresponding author.
E-mail address: yuxuebin@fudan.edu.cn (X. Yu).

Especially, the metal cation doping seems to be a common method used in a wide range of areas including the catalytic hydrolysis of AB. To exemplify, Kun Feng et al. reported the Co-doped CuO catalyst anchored on the Graphene Oxide [30] established a superior catalytic performance for AB hydrolysis with a high initial TOF value of 70.0 min^{-1}. Further characterization revealed the important synergetic effect of Co and Cu species contributed to the catalytic activity enhancement. Additionally, the effect of metal-ion doping in the phosphate was also explored by Chun-Chao Hou et al. [37] They found that the substantial improvement of the catalytic rate of Ni$_{2-x}$Co$_x$P after Co doping was resulted from the enhancement of interaction between catalyst and AB molecular, which can simultaneously facilitate the hydroxyl activation of AB. Recently there are several researches with CoP as the main object focused on building interface structures like Co$_3$B-CoP [38], and CoP-CoO [39,40], and this interface-exciting effect facilitates the targeted adsorption and activation of AB and H$_2$O molecules to generate H* and H$_2$. These findings demonstrate the importance of anionic regulation in efficient catalyst design. Nevertheless, the studies of anion doping engineering over transition metal-based compounds such as Co$_3$O$_4$ to ameliorate catalytic functions for AB hydrolysis are lacking, and the mechanism of catalyst materials and its catalytic behaviors for AB hydrolysis after anion doping is still unknown. Thus, an in-depth exploration of anion doping effect for catalyst materials is required.

Based on this scenario, we herein combine the nanoconfinement effect of material synthesis and anion modification strategy to design a highly efficient nanocatalyst for AB hydrolysis, and further investigate the catalytic performance and mechanism of ion doping effect. In details, the zeolitic imidazolate frameworks (ZIF-67) derived Co$_3$O$_4$ particles in a carbon-based nanoframeworks (named Co$_3$O$_4$@CNF) demonstrates a 29 times superior catalytic performance after a simple phosphorus anion doping in catalyzing AB hydrolysis. With various P doping content, the P2-Co$_3$O$_4$@CNF with moderate P content displays the best catalytic performance with an initial TOF value of 20.2 min^{-1} at 30 °C. Moreover, when combine normal copper-cation doping with the P doping, the P, Cu co-doped Co$_3$O$_4$@CNF catalyst can achieve a superior high TOF value of 35.6 min^{-1}, which is 51-fold of pure Co$_3$O$_4$@CNF, and hydrogen generation rate (HGR) of 15,002.3 mL$_{H2}$ min^{-1} g$_{metal}^{-1}$ for AB hydrolysis under the same conditions. The X-ray photoelectron spectroscopy (XPS), X-ray absorption fine structure (XAFS) and density functional theory (DFT) calculation results show that the electronic structure is modulated by P and Cu doping, including the variation of the electron density of the Co active sites and d-band center. So, the regulation of electronic structure on Co$_3$O$_4$ leads to the activated Co catalytic site and facilitate H$_2$O dissociation, thereby boosting AB hydrolysis.

2. Experimental section

2.1. Synthesis of ZIF-67, Cu(acac)2@ZIF-67, Ni(acac)2@ZIF-67, and Fe(C5H5)2@ZIF-67

For the synthesis of ZIF-67, Co(NO$_3$)$_2$·6H$_2$O (0.87 g, 3 mmol) were dissolved in 40 mL methanol to a clear solution. 2-MeIm (2-Methylimidazole, 1.31 g, 16 mmol) was dissolved in 20 mL methanol to form a clear solution. Then, the solution of 2-MeIm was subsequently poured into the solution of Co(NO$_3$)$_2$·6H$_2$O. After mixing and stirring at 30 °C for 24 h, the purple precipitates were centrifuged and washed with methanol three times and dried at 50 °C via dynamic vacuum on a Schlenk line. For the synthesis of Cu(acac)$_2$@ZIF-67, Cu(acac)$_2$ (copper acetylacetonate, 0.26 g, 1 mmol) were dissolved with Co(NO$_3$)$_2$·6H$_2$O at first and the other procedure was the same as ZIF-67. The Cu(acac)$_2$@ZIF-67 precursors with different Cu content were synthesized by adding different Cu(acac)$_2$ (0.5 mmol, and 1.5 mmol). Ni(acac)$_2$@-ZIF-67 and Fe(C$_5$H$_5$)$_2$@ZIF-67 can be synthesized by the same method with Cu(acac)$_2$@ZIF-67 except for with the change of Cu(acac)$_2$. For instance, Ni(acac)$_2$ (0.253 g, 1 mmol) for Ni(acac)$_2$@ZIF-67, Fe(C$_5$H$_5$)$_2$ (0.186 g, 1 mmol) for Fe(C$_5$H$_5$)$_2$@ZIF-67. was synthesized without the addition of Cu(acac)$_2$.

2.2. Synthesis of Co3O4@CNF and M-Co3O4@CNF (M = Cu, Ni, Fe)

The as-synthesized ZIF-67 Cu(acac)$_2$@ZIF-67, Ni(acac)$_2$@ZIF-67, and Fe(C$_5$H$_5$)$_2$@ZIF-67 were placed in a tube furnace and heated to 300 °C with a ramp rate of 2 °C min^{-1} and kept for 2 h in air to yield Co$_3$O$_4$@CNF and M-Co$_3$O$_4$@CNF (M = Cu, Ni, Fe), respectively.

2.3. Synthesis of Px-Co3O4@CNF and Px-Cu-Co3O4@CNF

The as-synthesized Co$_3$O$_4$@CNF (20 mg) and Cu-Co$_3$O$_4$@CNF (20 mg) were placed at the middle of a porcelain boat and 280 mg of NaH$_2$PO$_2$ was placed at the upstream side. The porcelain boat was put in a tube furnace and heated to 300 °C with a ramp rate of 2 °C min^{-1} and kept for 30 min in Ar to yield P2-Co$_3$O$_4$@CNF and P2-Cu-Co$_3$O$_4$@CNF. The Px-Co$_3$O$_4$@CNF and Px-Cu-Co$_3$O$_4$@CNF with different P content were synthesized by adding different NaH$_2$PO$_2$ (P1: 140 mg; P3: 420 mg).

2.4. Characterizations of catalysts

Powder X-ray diffraction pattern (PXRD) was carried out with a Rigaku D/max 2000 diffractometer with monochromatized Cu Kα radiation (λ = 1.5418 Å) at a scan rate of 10° min^{-1}. Scanning electron microscope (SEM) was performed on a Hitachi S-4800 electron microscope with acceleration voltage of 1 kV. Transmission electron microscope (TEM) was operated by a Hitachi-7700 working at 100 kV. HRTEM and HAADF-STEM were carried out by a JEOL JEM-2100F field emission electron microscope working at 200 kV. Atomic resolution HAADF-STEM images were obtained by using a Titan 80–300 scanning/ transmission electron microscope operated at 200 kV, equipped with a probe spherical aberration corrector. Inductively coupled plasma optical emission spectrometry (ICP-OES) was carried out on Thermo Fisher iCAP PRO. X-ray photoelectron spectroscopy (XPS) and Auger electron spectroscopy (AES) analysis were performed on a Thermo Scientific K-Alpha using 200 W monochromated Al Kα radiation. X-ray absorption fine structure (XAFS) spectroscopy was carried out using the RapidXAFS 1 M (Anhui Absorption Spectroscopy Analysis Instrument Co., Ltd.) by transmission mode at 25 kV and 40 mA, and the Si (533) spherically bent crystal analyzer with a radius of curvature of 500 mm was used.

2.5. Catalytic activity evaluation

For the hydrolytic dehydrogenation of AB, firstly a certain amount of catalysts (typically 6 mg for Px-Co$_3$O$_4$@CNF and 3 mg for Px-Cu-Co$_3$O$_4$@CNF) was added to a 50 mL two-necked flask containing 5 mL of water, followed by an ultrasonication treatment for 10 min. Then the flask reactor was kept at a certain temperature by a water bath. Finally, the reaction started when 2 mmol of AB dissolved in 1 mol L^{-1} NaOH aqueous solution (5 mL) was injected into the round-bottom flask by using a syringe under stirring conditions. The generated hydrogen passes through a drier to remove the water vapor, and the volume of H$_2$ was recorded by a flowmeter (Ritter MGC-1 V3.4 PMMA) connected with a computer. The hydrogen is exhausted to the outside to ensure safety. The reaction was completed when there was no more gas generated.

The catalytic activity of samples was evaluated by TOF value:

$$\text{TOF} = \frac{n_{H_2}}{n_{metal} * t} \tag{2}$$

in which n_{H_2} is the mole number of generated H$_2$, n_{metal} is the mole number of metal element in the catalysts, t is the reaction time in unit of minutes. For the stability experiments, the catalyst was recovered and reused for the next cycle under the same condition.

3. Results and discussion

3.1. Catalyst characterizations and catalytic performance

A gas-solid reaction method is developed to prepare P doped Co_3O_4@CNF (P*x*-Co_3O_4@CNF, *x* denotes the ratio of phosphorus source and precursor), as illustrated in Fig. 1a. In the first step, the Co_3O_4@CNF was synthesized by using ZIF-67 as the precursor heated at 300 °C for 2 h in air. Scanning electron microscopy (SEM) images show that the precursor ZIF-67 has a rhombic dodecahedral morphology with smooth surfaces, uniform size of 1 μm while the product Co_3O_4@CNF has a shrunken dodecahedral structure with uniform size around 500 nm (Fig. S1, Supporting Information). Then, P*x*-Co_3O_4@CNF products were prepared by using a facile PH_3 gas phosphating treatment on Co_3O_4@CNF. The morphology structure of the as-prepared products was characterized by SEM and transition electron microscopy (TEM) in Fig. 1b–d (Fig. S2, S3). Compared to Co_3O_4@CNF dodecahedra, the product P2-Co_3O_4@CNF shows a similar shrunken dodecahedral structure with uniform size around 500 nm, but the P2-Co_3O_4@CNF

dodecahedra has a smoother surface, indicating that a gas-solid reaction has occurred between Co_3O_4 and PH_3. X-ray diffraction (XRD) was used to investigate the crystal phase change before and after P incorporation. Fig. 1f shows that all of the diffraction peaks of P*x*-Co_3O_4@CNF are indexed to the typical cubic Co_3O_4 structure (JCPDS No. 42–1467) without impurity diffraction peaks, indicating that the successful P doping does not destroy the crystal structure of Co_3O_4. ICP-OES (Inductively coupled plasma optical emission spectrometry) results shown in Table S1 revealed the different Co content in the Co_3O_4. The high-resolution TEM (HRTEM) image (Fig. 1e) shows the lattice fringes with interplanar distances of 0.243 nm, corresponding to (311) planes of cubic Co_3O_4. This suggests that P2-Co_3O_4@CNF still maintains a cubic crystal phase, which corroborates with the XRD result. Moreover, the HAADF-STEM elemental mappings (Fig. 1g) present a homogeneous spatial distribution of Co, O, and P elements in the typical P2-Co_3O_4@CNF dodecahedra, demonstrating the successful doping of the P element. In addition, the homogeneous distribution of N and C elements confirms the existence of carbon skeleton derived from ZIF pyrolysis [41].
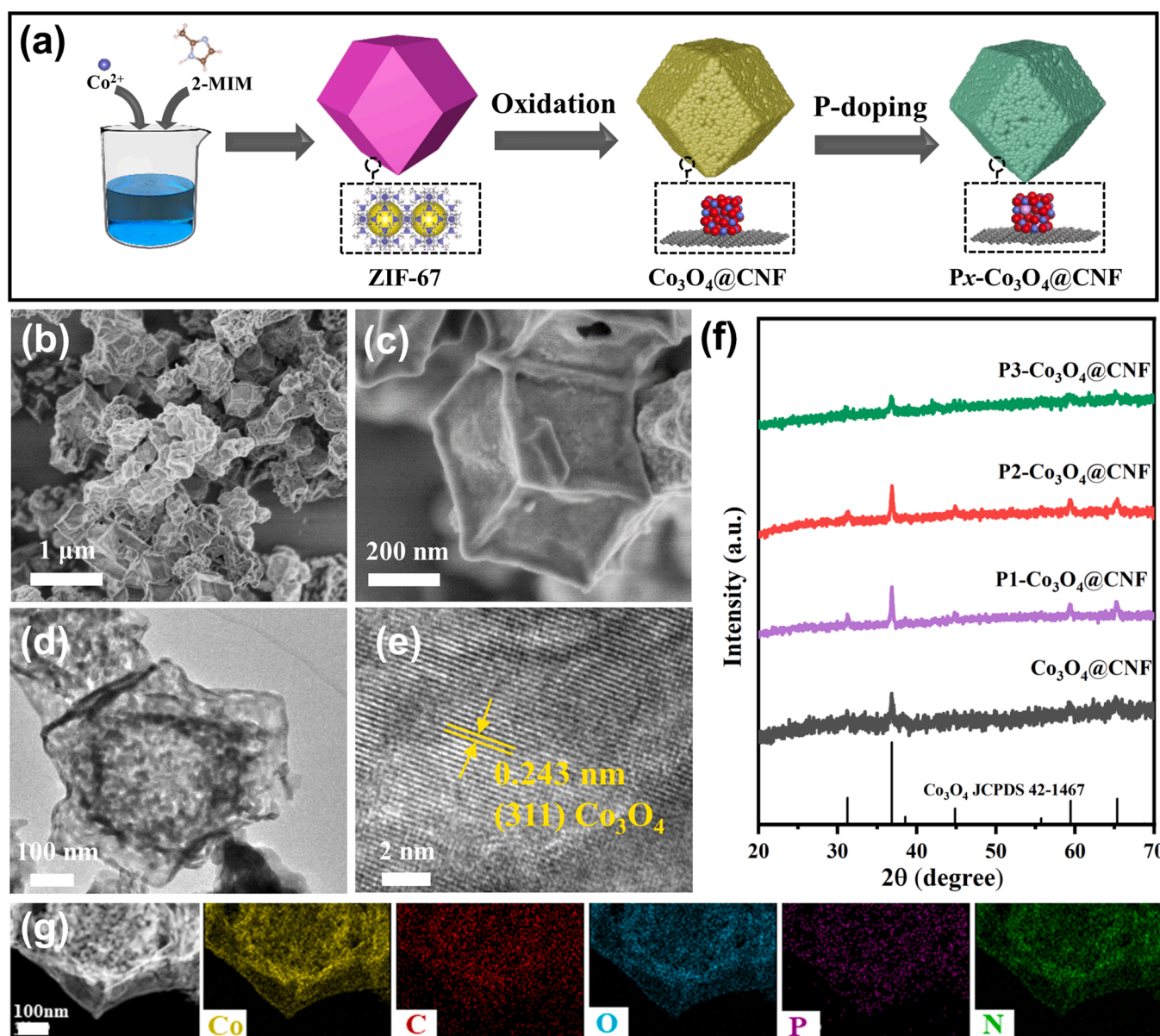

Fig. 1. (a) The preparation procedure of the P*x*-Co_3O_4@CNF sample. (b, c) SEM, (d) TEM and (e) HRTEM images of the as-prepared P2-Co_3O_4@CNF. (f) XRD patterns of the Co_3O_4@CNF and different P content P-Co_3O_4@CNF. (g) EDS elemental mapping images of the P2-Co_3O_4@CNF.

To evaluate the catalytic activity of the Px-Co$_3$O$_4$@CNF, the hydrogen generation reaction from AB hydrolysis catalyzed by various catalysts was first tested via a sealed flask equipped with a magnetic stirrer under ambient conditions. According to the results in Fig. 2a, b, the P2-Co$_3$O$_4$@CNF catalyst exhibited the highest activity for hydrogen release amongst the investigated catalysts. 6 mmol hydrogen generated from the hydrolysis of 2 mmol AB is achieved within 5 min by the catalyzing of P2-Co$_3$O$_4$@CNF. And the TOF value of Co$_3$O$_4$@CNF, P1-Co$_3$O$_4$@CNF, P2-Co$_3$O$_4$@CNF, P3-Co$_3$O$_4$@CNF is 0.7, 14.8, 20.2 and 7.4 min^{-1}, respectively. It should be noted that the measured activity exhibits a volcano-like dependence on the P content in a series of Px-Co$_3$O$_4$@CNF catalysts. Moreover, the TOF value of fully phosphatized CoP@CNF for catalyzing the AB hydrolysis is 14.9 min^{-1}, which was also lower than that of P2-Co$_3$O$_4$@CNF (Fig. S4), further illustrating the enhancement of P doping on the catalyst properties. As shown in Fig. 2c, d, we also investigated the temperature dependence of the P2-Co$_3$O$_4$@CNF catalytic reaction in the range of 293–313 K. The activation energy is estimated to be 37.65 KJ mol^{-1} through an Arrhenius plot. This value is favourably comparable to some of noble metal based catalysts [26,42,43]. Compared with pure Co$_3$O$_4$@CNF, the activation energy of Co$_3$O$_4$@CNF with 69.67 KJ mol^{-1} is much higher than P2-Co$_3$O$_4$@CNF (Fig. S5), indicating that the catalytic performance of the material was greatly improved after phosphorus doping. Obviously, the successful doping of phosphorus significantly improves the catalytic performance of Co$_3$O$_4$@CNF from thermodynamic and kinetic perspectives, demonstrating the effectiveness of the anion doping strategy.

3.2. Synergistic modulation strategy

Furthermore, an anion and cation co-doping strategy was adopted to improve the catalytic activity of Co$_3$O$_4$@CNF. Firstly, a self-templating transformation (STT) strategy [44,45] was developed to synthesize metal cation doped Co$_3$O$_4$@CNF (M-Co$_3$O$_4$@CNF, M = Cu, Ni, Fe) from metal precursor@ZIF-67. From the SEM, TEM and XRD results in Fig. S6-S8, after metal cation doping, the M-Co$_3$O$_4$@CNF maintains a similar polyhedral morphology and unaltered typical cubic phase, indicating the successful doping engineering. Preliminary performance test results show that the Cu-Co$_3$O$_4$@CNF has the best catalytic performance with TOF of 10.5 min^{-1} while Ni-Co$_3$O$_4$@CNF and Fe-Co$_3$O$_4$@CNF was 0.5 min^{-1} and 0.6 min^{-1}, respectively (Fig. S9a). The catalytic performance of Cu-doped samples is found to be less affected by the doping content of Cu, and the sample with the optimal doping content is Cu-Co$_3$O$_4$@CNF (Fig. S9b). Additionally, after metal cation and phosphorus anion co-doping, improved properties are achieved and the Cu, P co-doped has the best catalytic performance (Fig. S10). Therefore, we take the Cu/P co-doped samples as the main research object to explore the synergistic effect brought by the co-doping of Cu and P. As shown in Fig. 3a–c, after P doping treatment, the dodecahedra morphology of P2-Cu-Co$_3$O$_4$@CNF (Px-Cu-Co$_3$O$_4$@CNF means P, Cu co-doped Co$_3$O$_4$@CNF, x denotes the ratio of phosphorus source and precursor)) is further shrunk because of the reaction with PH$_3$. To determine the crystal change of the Co$_3$O$_4$@CNF after Cu, P co-doping, XRD patterns were performed as shown in Fig. 3e. The XRD of Px-Cu-Co$_3$O$_4$@CNF and Cu-Co$_3$O$_4$@CNF show similar peaks with ZIF-67-derived Co$_3$O$_4$@CNF, and the peaks at 31.1°, 36.7°, 59.1°, and 65.0° can be attributed to (220), (311), (511), and (440) lattice planes of
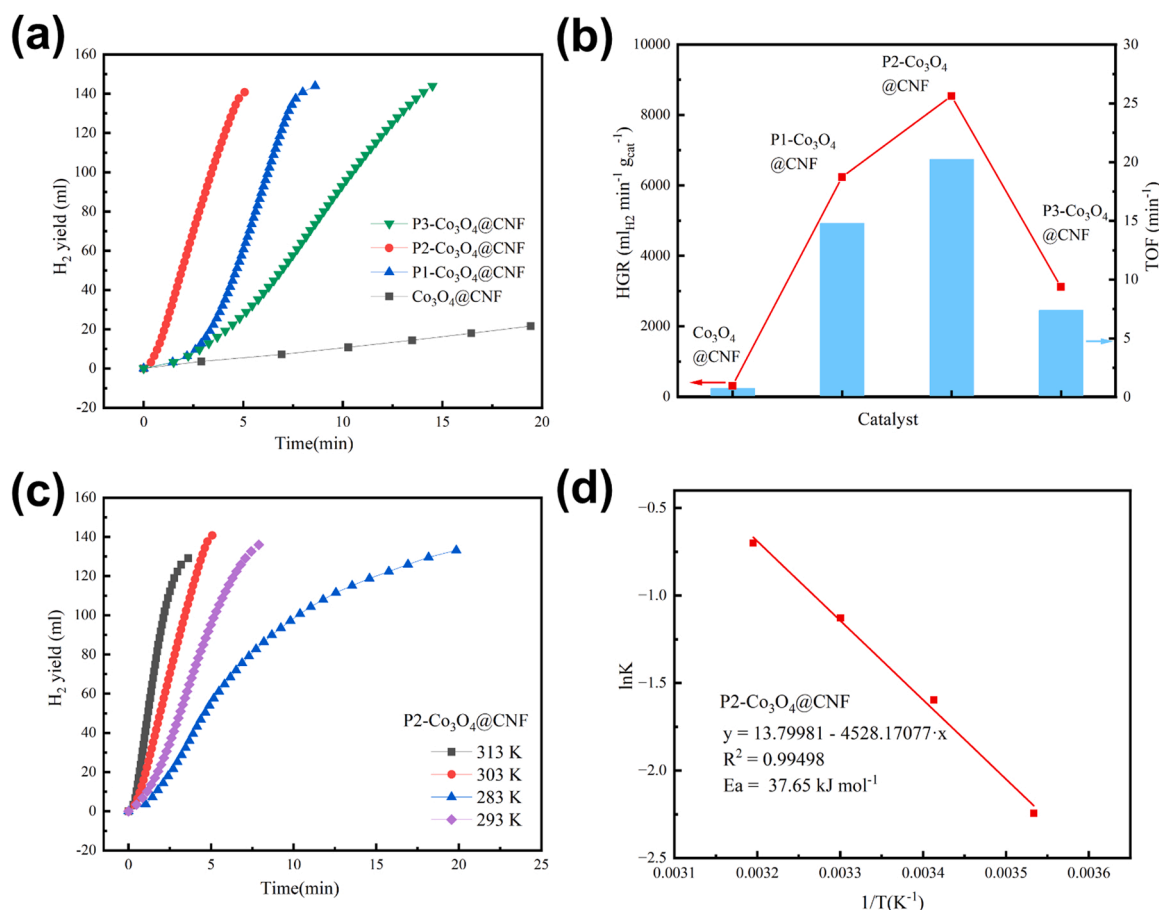
Fig. 2. Hydrogen generation catalyzed by (a) Co$_3$O$_4$@CNF, P1-Co$_3$O$_4$@CNF, P2-Co$_3$O$_4$@CNF, P3-Co$_3$O$_4$@CNF at 303 K, and (b) corresponding hydrogen generation rates and TOF value. Hydrogen evolution from AB dehydrogenation catalyzed by (c) P2-Co$_3$O$_4$@CNF at different temperatures and (d) corresponding Arrhenius plot.
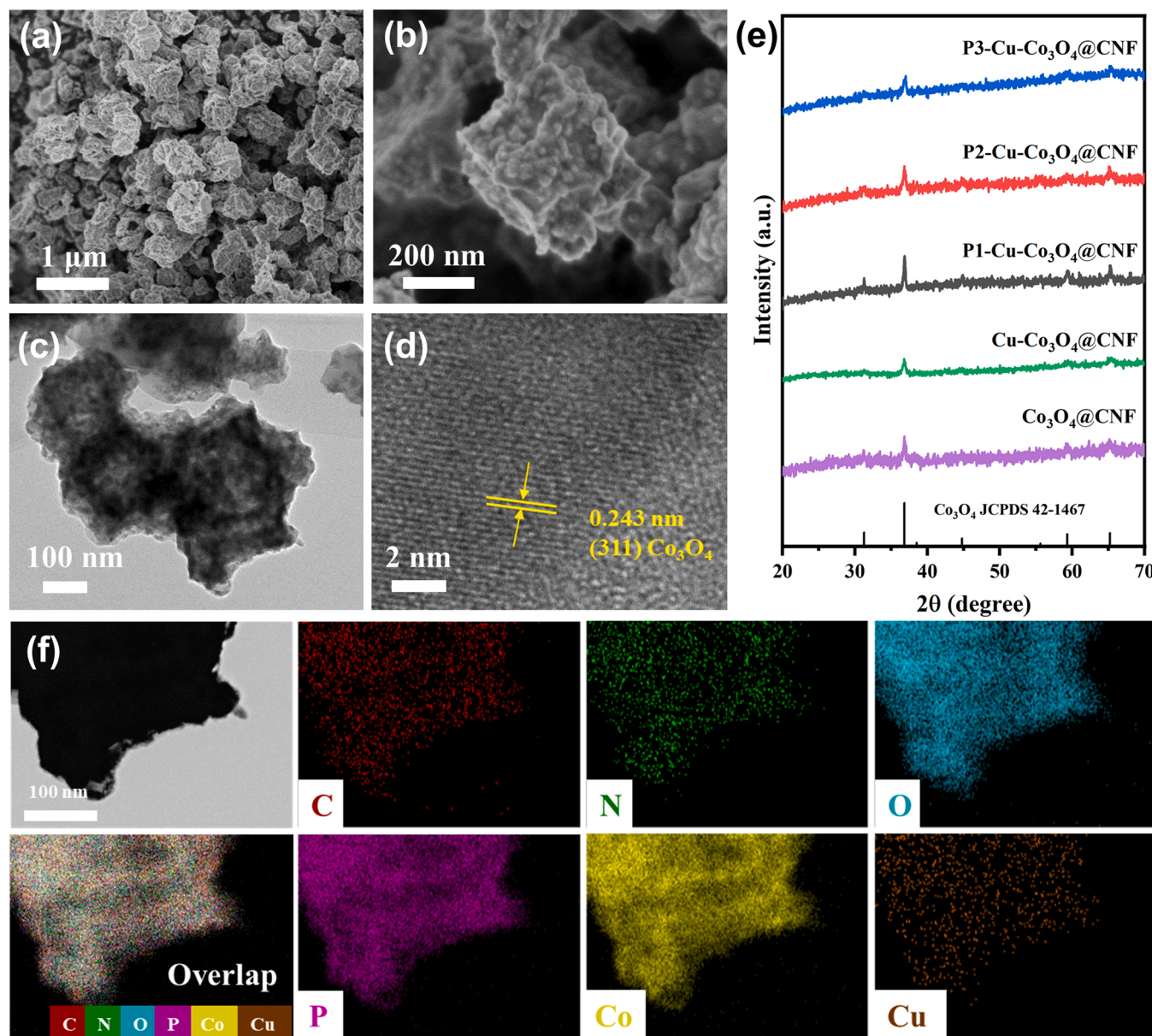
Fig. 3. (a, b) SEM, (c) TEM and (d) HRTEM images of the as-prepared P2-Cu-Co$_3$O$_4$@CNF. (e) XRD patterns of the Cu-Co$_3$O$_4$@CNF and different P content Px-Cu-Co$_3$O$_4$@CNF. (f) EDS elemental mapping images of the P2-Cu-Co$_3$O$_4$@CNF.

Co$_3$O$_4$, respectively, suggesting successful Cu and P doping into the lattice of Co$_3$O$_4$ without phase destruction and impurity generation. The HRTEM image of the P2-Cu-Co$_3$O$_4$@CNF was showed in Fig. 3d, and the measured lattice fringe distance is approximately 0.243 nm, which consists with the Co$_3$O$_4$ (311) plane. Moreover, HAADF-STEM and EDS elemental mapping (Fig. 3f) also confirmed that all the elementals including O, P, Co, Cu were uniformly distributed over the fractional dodecahedra after doping. These results are consistent with the XRD results, demonstrating the successful doping of Cu and P cation. Also, the homogeneous distribution of N and C elements signifies the carbon nanoframwork derived from ZIF-67 pyrolysis [41]. ICP-OES results shown in Table S1 also quantitatively revealed the different P doping content and Cu doping content into the Co$_3$O$_4$.

The catalytic activity of various Px-Cu-Co$_3$O$_4$@CNF samples in the hydrolysis of AB was evaluated as shown in Fig. 4a-b. Similar with Px-Co$_3$O$_4$@CNF, Px-Cu-Co$_3$O$_4$@CNF follows the same rules. The measured activity of a series of Px-Cu-Co$_3$O$_4$@CNF catalysts also exhibits a volcano-like dependence on the P doping content. Among the

investigated catalysts, the P2-Cu-Co$_3$O$_4$@CNF catalyst exhibited the highest activity for hydrogen release with a superior TOF of 35.6 min-1 and a superb HGR of 15002.3 mL$_{H2}$ min^{-1} g$_{metal}^{-1}$ while the TOF and HGR of Cu-Co$_3$O$_4$@CNF was 10.5 min^{-1} and 4414.6 mL$_{H2}$ min^{-1} g$_{metal}^{-1}$. In contrast, the TOF and HGR of P1-Cu-Co$_3$O$_4$@CNF and P3-Cu-Co$_3$O$_4$@CNF was 16.7, 17.1 min^{-1} and 7067.4, 7208.2 mL$_{H2}$ min^{-1} g$_{metal}^{-1}$, respectively. The catalytic performance of all P-doped samples is obviously superior to that of bare Cu-Co$_3$O$_4$@CNF, indicating that the surprising promotion effect of P doping strategy. More importantly, in Fig. 4c, even compared to fully phosphated samples Cu-CoP@CNF with a TOF of 18.8 min^{-1}, P2-Cu-Co$_3$O$_4$@CNF displayed a better catalytic performance with nearly twice that of Cu-CoP@CNF. The performance improvement brought by a small amount of P doping has exceeded the catalytic activity of the phosphide itself, further illustrating the effectiveness of the phosphorus doping strategy. Fig. 4d-f shows the catalytic performance of pure Co$_3$O$_4$@CNF and Cu- Co$_3$O$_4$@CNF, P2-Co$_3$O$_4$@CNF and P2-Cu-Co$_3$O$_4$@CNF for AB hydrolysis. Obviously, their catalytic activities are as follows: P2-Cu-Co$_3$O$_4$@CNF (TOF = 35.6 min^{-1}) > P2-
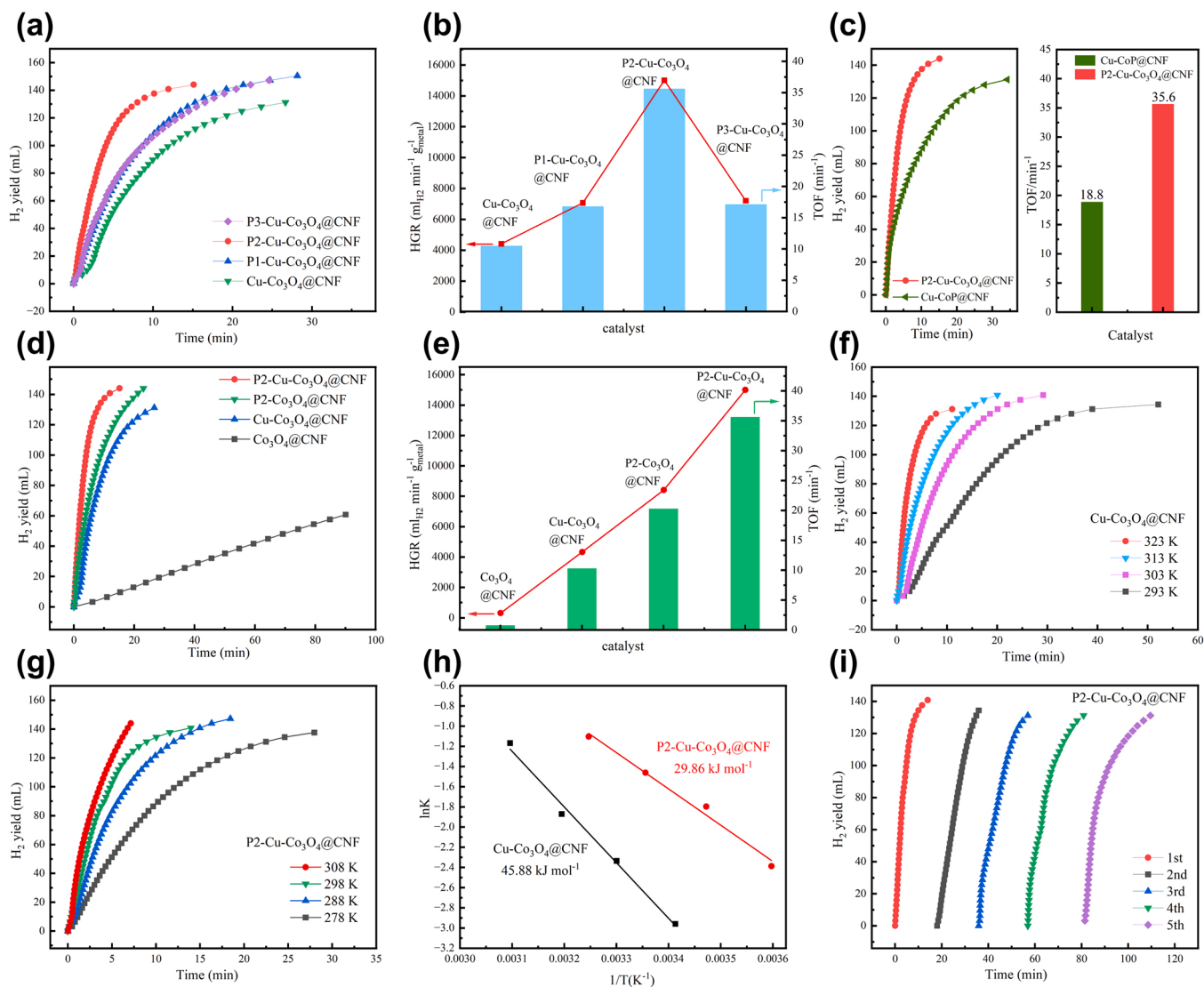
Fig. 4. Hydrogen generation catalyzed by (a) Cu-Co$_3$O$_4$@CNF, P1-Cu-Co$_3$O$_4$@CNF, P2-Cu-Co$_3$O$_4$@CNF and P3-Cu-Co$_3$O$_4$@CNF at 303 K. (b) Corresponding hydrogen generation rates and TOF value. Hydrogen evolution from AB dehydrogenation catalyzed by (c) P2-Cu-Co$_3$O$_4$@CNF and Cu-CoP@CNF at 303 K and the corresponding TOF value. Hydrogen generation catalyzed by (d) Co$_3$O$_4$@CNF, Cu-Co$_3$O$_4$@CNF, P2-Co$_3$O$_4$@CNF and P2-Cu-Co$_3$O$_4$@CNF at 303 K. (e) Corresponding hydrogen generation rates and TOF value. Hydrogen evolution from AB dehydrogenation catalyzed by (f) Cu-Co$_3$O$_4$@CNF, (g) P2-Cu-Co$_3$O$_4$@CNF at different temperatures and (h) the corresponding Arrhenius plot. (i) Durability test of P2-Cu-Co$_3$O$_4$@CNF at 303 K while catalyzing 2 mmol of AB in each cycle.

Co$_3$O$_4$@CNF (TOF = 20.2 min^{-1}) > Cu-Co$_3$O$_4$@CNF (TOF = 10.5 min^{-1}) > pure Co$_3$O$_4$@CNF (TOF = 0.7 min^{-1}). The catalytic activity of P2-Co$_3$O$_4$@CNF is about 2 times that of Cu-Co$_3$O$_4$@CNF, indicating the anionic doping is more effective and important than cationic doping to some extent. Additionally, the performance of the co-doped samples is much higher than that of the samples doped with copper or phosphorus alone, illustrating the strong synergistic boosting effect produced by the co-doping.

The measure of the time dependence of hydrogen generation at various temperatures was showed in Fig. 4f–h, revealed a much lower apparent activation energy of 29.86 KJ mol^{-1} on P2-Cu-Co$_3$O$_4$@CNF than that of 45.88 KJ mol^{-1} on Cu-Co$_3$O$_4$@CNF and 37.65 KJ mol^{-1} on P2-Co$_3$O$_4$@CNF, further indicating the strong synergistic implication by the Cu, P co-doping from a kinetic view. The TOF and Ea of the reported catalysts are listed in Table S2. This TOF and Ea value show that the catalytic performance of P2-Cu-Co$_3$O$_4$@CNF has a certain competitive advantage over the reported non-noble metal catalyst. Recycling stability of the catalyst is another critical parameter for its practical application. The continuous recycling test of the AB hydrolysis over the

P2-Cu-Co$_3$O$_4$@CNF sample was performed at 303 K. As depicted in Fig. 4i, the catalyst was reused for 5 cycles of 2 mmol AB per cycle without significant catalytic activity degradation. The observed slight drop in activity could be ascribed to continuous adsorption of borates on the active sites [34,46,47]. To explore the role of NaOH, the hydrogen production in the absence of NaOH was carried out under the same conditions. As shown in Fig. S11, NaOH provides a positive role as a catalytic promoter in AB hydrolysis.

3.3. Mechanism analysis

Encouraged by the superior catalytic performance of P2-Cu-Co$_3$O$_4$@CNF catalyst, the difference in the electronic properties between pure and ion-doped catalysts was first studied by the XPS. The XPS survey pattern of P2-Co$_3$O$_4$@CNF and P2-Cu-Co$_3$O$_4$@CNF shows an obvious P 2p signal after the doping of elemental P (Fig. 5b, Fig. S12 in the Supporting Information). Fig. 5c shows an obvious Cu 2p signal in XPS results of Cu-Co$_3$O$_4$@CNF and P2-Cu-Co$_3$O$_4$@CNF after elemental Cu doping. These results agree with those described above,
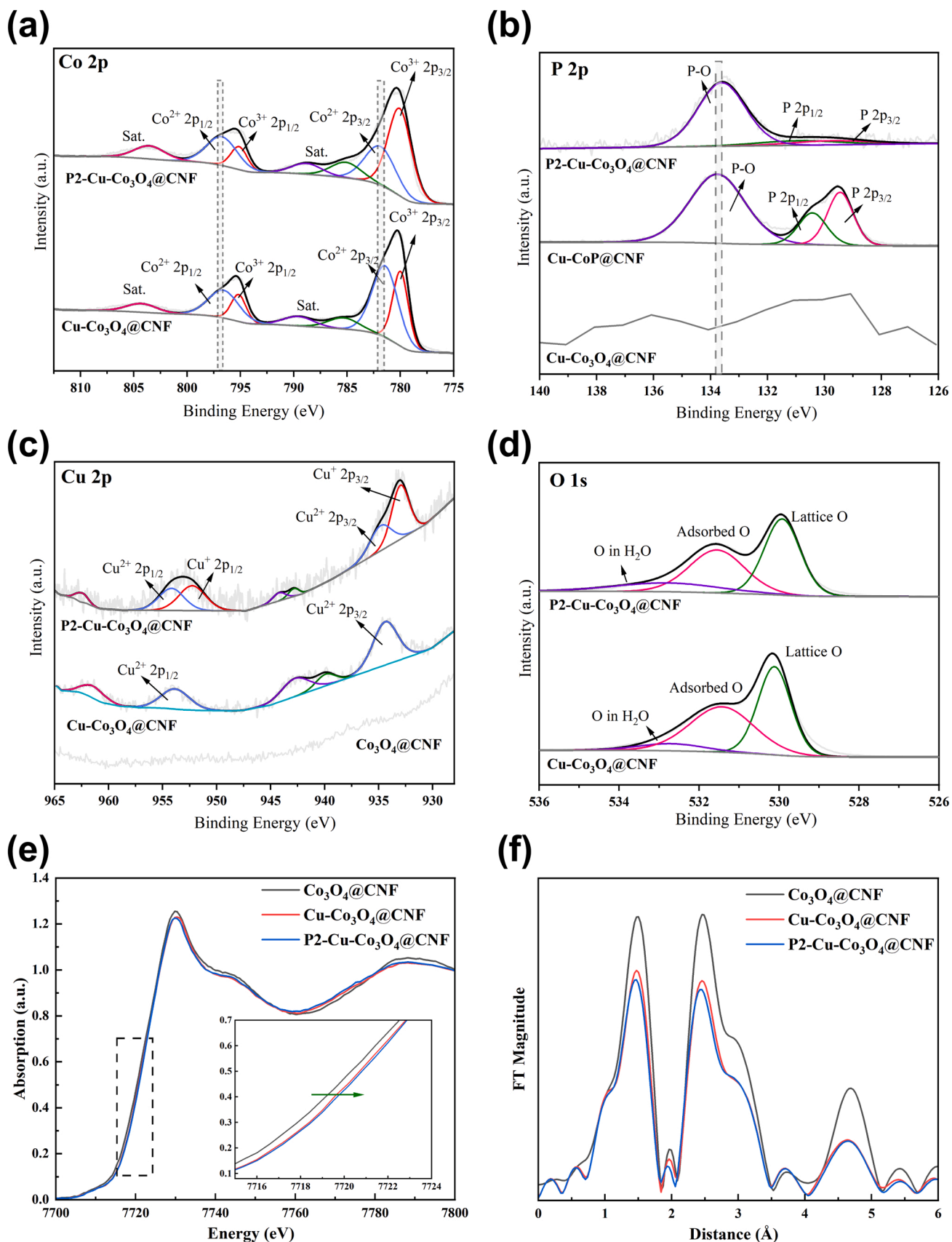
Fig. 5. Fine XPS spectra of (a) Co 2p, (b) P 2p, (c) Cu 2p and (d) O 1s of Co_3O_4@CNF, Cu-Co_3O_4@CNF, P2-Cu-Co_3O_4@CNF and Cu-CoP@CNF samples. (e) Co K-edge XANES and (f) FT-EXAFS curves of Co_3O_4@CNF, Cu-Co_3O_4@CNF and P2-Cu-Co_3O_4@CNF samples.

demonstrating the successful elemental doping. In the Co 2p high-resolution region of P2-Cu-Co$_3$O$_4$@CNF (Fig. 5a), the peaks at 781.0 and 796.7 eV with satellites (abbreviated as "Sat.") are fitted to reveal Co^{2+} cation, and two peaks located at 779.7 and 794.9 eV should be assigned to the Co^{3+} configuration, which indicates the coexistence of the Co^{2+} and Co^{3+}. It can be seen that the Co 2p peaks for both P2-Cu-Co$_3$O$_4$@CNF and P2-Co$_3$O$_4$@CNF samples display a positive shift with higher binding energies (Fig. S13b), compared with pristine Cu-Co$_3$O$_4$@CNF and Co$_3$O$_4$@CNF, and the increased relative atomic ratio of Co^{3+}/Co^{2+} suggests a lower electron density around Co atoms after introducing P. As for Cu doping effect, when compared Cu-Co$_3$O$_4$@CNF with Co$_3$O$_4$@CNF (Fig. S13a), we should note that the Co 2p peaks were shifted slightly to a higher binding energy, implying the decrease of the electron density for Co species. In the P 2p high-resolution region (Fig. 5b, Fig. S13c), the sub-peaks of P 2p$_{1/2}$ (130.9 eV), P 2p$_{3/2}$ (129.7 eV) and P-O (133.6 eV) of P2-Cu-Co$_3$O$_4$@CNF indicate the successful doping of P element into Cu-Co$_3$O$_4$@CNF sample. In addition, compared with fully phosphated Cu-CoP@CNF and CoP@CNF samples,

the P-O peak slightly shifts to lower binding energy, suggesting a higher electron density around P atoms in the P2-Cu-Co$_3$O$_4$@CNF and P2-Co$_3$O$_4$@CNF samples. In addition, the observed peaks of Cu^{2+} (934.8 eV, 954.2 eV), and Cu$^+$ (933.0 eV, 952.3 eV) for P2-Cu-Co$_3$O$_4$@CNF in Fig. 5c indicate the successful doping of Cu element [48, 49]. And the Cu$^+$ species in P2-Cu-Co$_3$O$_4$@CNF may be due to the reduction of Cu^{2+} by sodium hypophosphite (Fig. S14). In the O 1s region of XPS spectra for P2-Cu-Co$_3$O$_4$@CNF and Cu-Co$_3$O$_4$@CNF in Fig. 5d (for P2-Co$_3$O$_4$@CNF and Co$_3$O$_4$@CNF in Fig. S13d), the fitted peaks at 529.9, 531.6, and 532.8 eV are attributed to lattice O from metal−oxygen bonds, adsorbed O from surface hydroxy and/or adsorbed oxygen species, and O from the surface of absorbed H$_2$O for P2-Cu-Co$_3$O$_4$@CNF, respectively. The ratio of adsorbed O/lattice O was increased after P doping treatment, indicating the partial replacement of lattice O by P atom in Co$_3$O$_4$.

To further identify the electronic structure modulation of P2-Cu-Co$_3$O$_4$@CNF, the XAFS is collected. The Co K-edge X-ray absorption near-edge structure (XANES) of Co$_3$O$_4$@CNF, Cu-Co$_3$O$_4$@CNF and P2-

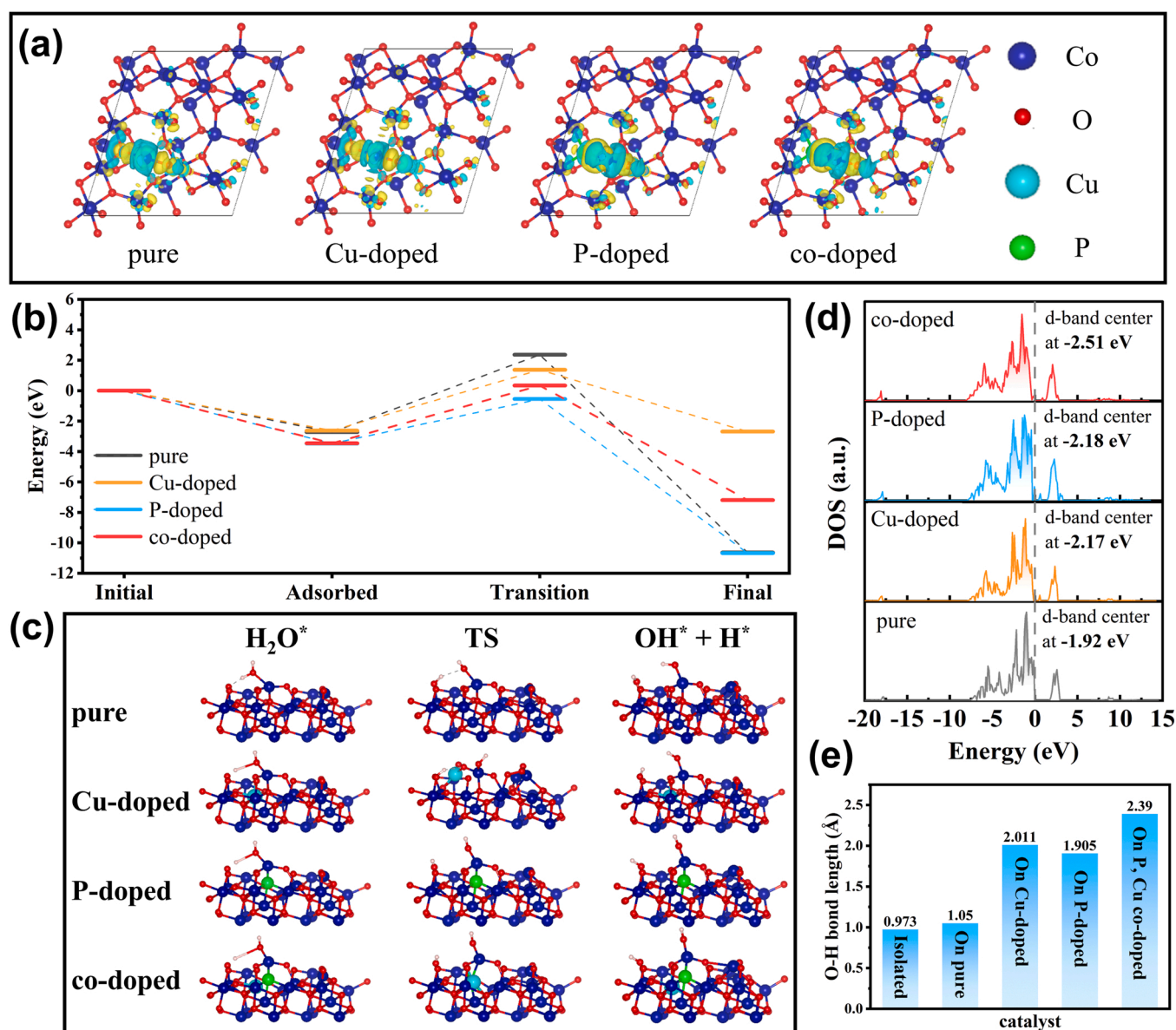**Fig. 6.** (a) Charge density difference maps of pure and modified Co$_3$O$_4$ (311) slabs. (b) Energy profiles of H$_2$O dissociation on different catalysts and (c) corresponding optimized 3D structures of adsorbed H$_2$O(H$_2$O*), transition state (TS) and final products (OH*+H*). (d) DOS of Co 3d in pure and modified Co$_3$O$_4$. (e) O-H bond length of adsorbed H$_2$O on pure and modified Co$_3$O$_4$ (311) slabs.

Cu-Co₃O₄@CNF are shown in Fig. 5e. The Co K-edge curve of doped sample is similar to that of pure Co_3O_4, which confirms that no new phase is generated after Cu or P incorporation. Moreover, the absorption edge of doped sample shifts toward a higher binding energy compared with that of Co₃O₄@CNF, demonstrating the average valence state of Co in the sample follows this law: P2-Cu-Co₃O₄@CNF > Cu-Co₃O₄@CNF > Co₃O₄@CNF[50]. The increased average valence state implies the reduced electron density of the Co atom after Cu or P doping, and the co-doped samples have more obvious electronic structure modification effect, agreeing well with the XPS result. The Fourier transforms of the k^3-weighted EXAFS oscillations (FT-EXAFS) at the Co K-edge for all samples are shown in Fig. 5f. The unified strongest peaks correspond to the nearest Co−O bond [51]. Especially, the intensity of the doped samples displays an obvious decrease relative to that of Co₃O₄@CNF and the co-doped samples is relatively minimal, suggesting the reduced O coordination number of Co sites owning to the doping of Cu and P.

Therefore, it is not hard to draw a conclusion from the XPS and XAFS analysis results that the electronic structure of Co was modulated by introducing P anion and Cu cation. Specifically, the electrons around the Co atoms were partially transferred to the P atoms after P doping, as well as the doping of Cu cation, leading to a decrease in the electron density around Co, which can generate enriched empty d orbitals to promote the adsorption of OH group and H atom. Based on this modulation effect, the catalytic performance of doped samples has been greatly improved.

DFT calculations were further carried out to understand the underlying mechanism. The modulation of the doped ion on the electronic structure of Co_3O_4 was further confirmed by the charge difference maps (Fig. 6a), obviously, Cu and P atoms significantly change the electronic structure of catalysts. On co-doped Co₃O₄(311) surface, Co active sites are more positively charged than on pristine one, leading to an easier adsorption for reactors with lone pair electrons like OH group and H atom, which is in agreement with the results of the XPS and XAFS analyzation (Fig. 5). DOS of pure Co_3O_4, after Cu doping, P doping and Cu, P co-doping, shows a downshift of the d-band center from − 1.92 to − 2.17, − 2.18, and − 2.51 eV, respectively (Fig. 6d). The d band center theory indicates that the decrease of d-band center lead to a decrease of the binding strength between the adsorbate H and surface and facilitates the desorption of H from catalyst surface for AB hydrolysis.

On the other part, it has been reported that apart from H_2O adsorption step, the following H_2O cleavage is also an important step for AB hydrolytic dehydrogenation and regarded as the rate-determining step (RDS) [52–54]. Besides, we discovered that the hydrogen generation rate decreases dramatically in deuterated water (D_2O) of P2-Cu-Co₃O₄@CNF and the kinetic isotope effect (KIE) is 3.2 (Fig. S15). This observation implies that the cleavage of the O−H bond in H_2O is more likely to be the RDS. Hence, detailed reaction pathways and corresponding energy profiles (Fig. 6b, c) of H_2O decomposition on pure and modified catalysts' surfaces are performed. It is obviously that the reaction barrier on P-doped Co₃O₄(311) surface with 2.93 eV is much lower than on pure Co_3O_4(311) surface with 5.09 eV, indicating the enhancement of P doping effect. The lower reaction barrier on Cu-doped Co₃O₄(311) surface with 4.00 eV also indicates the improvement of Cu doping effect. Furthermore, Cu, P co-doped Co₃O₄(311) surface has a lowest reaction barrier of 3.80 eV compared with pure Co_3O_4 and Cu-doped Co_3O_4, implying the excellent thermodynamic promotion effect of Cu, P co-doping. However, even though P-doped Co_3O_4 exhibits a best thermodynamic condition, the adsorption energy (−10.68 eV) in the final state of P-doped Co₃O₄(311) is highest which is detrimental to final hydrogen desorption among all samples. Based on the above consideration, it can be concluded that the Cu, P co-doped catalyst combines the advantages of single-doped ones with mild reaction energy barrier and moderate adsorption strength so that the co-doped Co_3O_4 presents the most outstanding catalysis performance in AB hydrolysis. O-H bond length in adsorbed H_2O on different surfaces are also measured (Fig. 6e). A longest O-H bond (2.39 Å) is observed in H_2O on co-doped Co₃O₄(311) surface, which visually shows the weaken of O-H

bond and illustrates the excellent catalysis effect of co-doped Co_3O_4 more clearly.

4. Conclusion

In summary, we have combined a ZIF-67 derived nanoconfinement method and a facile ion doping approach to obtain a highly efficient Co_3O_4 catalyst for hydrogen generation from AB hydrolysis. Based on the strong enhancement of P doping effect, we have demonstrated a significant synergistic modulation with P and Cu co-doping strategy and the obtained P2-Cu-Co₃O₄@CNF exhibits the superior catalytic properties with a TOF of 35.6 min^{-1} which is 51 times that of pure Co₃O₄@CNF. Thermodynamic analysis showed that the apparent activation energy with 29.86 KJ mol^{-1} of P2-Cu-Co₃O₄@CNF is even lower than some other reported noble-metal based catalyst. Furthermore, we disclose the promotion mechanism of ion doping effect and discover that the incorporation of a small amount of P atoms into the Co_3O_4 will result in a strong electronic coupling between Co cation and P anion, which is similar to the Cu doping effect, and thus bring electronic structure regulation and a downshift of d-band, which are beneficial for not only accelerating the dissociation of water molecules but also optimizing the hydrogen desorption energy on catalyst surfaces. This work provides atomic-level insight into the relationship between the structure and properties and introduces a controllable way to modulate the electronic structure of catalysts toward designing high-efficient and earth-abundant catalysts.

CRediT authorship contribution statement

Chongyang Yuan: Investigation, Formal analysis, Data curation, Writing – original draft. **Tian Xu:** Data curation, Software, Writing – original draft. **Miao Guo:** Investigation, Formal analysis. **Tengfei Zhang:** Investigation, Formal analysis, Writing – review & editing, Funding acquisition. **Xuebin Yu:** Conceptualization, Writing – review & editing, Supervision, Funding acquisition.

Declaration of Competing Interest

The authors declare that they have no known competing financial interests or personal relationships that could have appeared to influence the work reported in this paper.

Data Availability

Data will be made available on request.

Acknowledgements

Appendix A. Supporting information

Supplementary data associated with this article can be found in the online version at doi:10.1016/j.apcatb.2022.122044.

References

[1] M.S. Dresselhaus, I.L. Thomas, Alternative energy technologies, Nature 414 (2001) 332–337, https://doi.org/10.1038/35104599.

[2] S. Wu, N. Salmon, M.M.-J. Li, R. Bañares-Alcántara, S.C.E. Tsang, Energy decarbonization via green H_2 or NH_3? ACS Energy Lett. 7 (2022) 1021–1033, https://doi.org/10.1021/acsenergylett.1c02816.

[3] L. Van Hoecke, L. Laffineur, R. Campe, P. Perreault, S.W. Verbruggen, S. Lenaerts, Challenges in the use of hydrogen for maritime applications, Energy Environ. Sci. 14 (2021) 815–843, https://doi.org/10.1039/d0ee01545h.

[4] X. Yu, Z. Tang, D. Sun, L. Ouyang, M. Zhu, Recent advances and remaining challenges of nanostructured materials for hydrogen storage applications, Prog. Mater. Sci. 88 (2017) 1–48, https://doi.org/10.1016/j.pmatsci.2017.03.001.

[5] C. Wang, D. Astruc, Recent developments of nanocatalyzed liquid-phase hydrogen generation, Chem. Soc. Rev. 50 (2021) 3437–3484, https://doi.org/10.1039/D0CS00515K.

[6] C. Lang, Y. Jia, X. Yao, Recent advances in liquid-phase chemical hydrogen storage, Energy Storage Mater. 26 (2020) 290–312, https://doi.org/10.1016/j.ensm.2020.01.010.

[7] Q. Sun, N. Wang, Q. Xu, J. Yu, Nanopore-supported metal nanocatalysts for efficient hydrogen generation from liquid-phase chemical hydrogen storage materials, Adv. Mater. 32 (2020), e2001818, https://doi.org/10.1002/adma.202001818.

[8] J. Yao, L. Guo, P. Zhu, F. Yang, H. Yan, S. Kurko, V.A. Yartys, Z. Zhang, Z. Wu, A multi-function desalination system based on hydrolysis reaction of hydride and fuel cell water recovery, Energy Convers. Manag. 247 (2021), 114728, https://doi.org/10.1016/j.enconman.2021.114728.

[9] W.-W. Zhan, Q.-L. Zhu, Q. Xu, Dehydrogenation of ammonia borane by metal nanoparticle catalysts, ACS Catal. 6 (2016) 6892–6905, https://doi.org/10.1021/acscatal.6b02209.

[10] L. Ouyang, J. Jiang, K. Chen, M. Zhu, Z. Liu, Hydrogen production via hydrolysis and alcoholysis of light metal-based materials: a review, Nano-Micro Lett. 13 (2021) 134, https://doi.org/10.1007/s40820-021-00657-9.

[11] S. Zhang, M. Li, L. Li, F. Dushimimana, J. Zhao, S. Wang, J. Han, X. Zhu, X. Liu, Q. Ge, H. Wang, Visible-light-driven multichannel regulation of local electron density to accelerate activation of O-H and B–H bonds for ammonia borane hydrolysis, ACS Catal. (2020) 14903–14915, https://doi.org/10.1021/acscatal.0c03965.

[12] Z. Tang, H. Chen, X. Chen, L. Wu, X. Yu, Graphene oxide based recyclable dehydrogenation of ammonia borane within a hybrid nanostructure, J. Am. Chem. Soc. 134 (2012) 5464–5467, https://doi.org/10.1021/ja300003t.

[13] H. Huang, C. Wang, Q. Li, R. Wang, Y. Yang, A. Muhetaer, F. Huang, B. Han, D. Xu, Efficient and full-spectrum photothermal dehydrogenation of ammonia borane for low-temperature release of hydrogen, Adv. Funct. Mater. 31 (2020) 2007591, https://doi.org/10.1002/adfm.202007591.

[14] C.D. Mboyi, D. Poinsot, J. Roger, K. Fajerwerg, M.L. Kahn, J.-C. Hierso, The hydrogen-storage challenge: nanoparticles for metal-catalyzed ammonia borane dehydrogenation, Small 17 (2021) 2102759, https://doi.org/10.1002/smll.202102759.

[15] C.Y. Peng, C.C. Hou, Q.Q. Chen, C.J. Wang, X.J. Lv, J. Zhong, W.F. Fu, C.M. Che, Y. Chen, Cu(OH)(2) supported on Fe(OH)(3) as a synergistic and highly efficient system for the dehydrogenation of ammonia-borane, Sci. Bull. 63 (2018) 1583–1590, https://doi.org/10.1016/j.scib.2018.11.003.

[16] X. Li, Q. Yao, Z. Li, H. Li, Q.-L. Zhu, Z.-H. Lu, Porphyrin framework-derived N-doped porous carbon-confined Ru for NH3BH3 methanolysis: the more pyridinic-N, the better, J. Mater. Chem. A 10 (2022) 326–336, https://doi.org/10.1039/D1TA06807E.

[17] Q. Wang, F. Fu, S. Yang, M. Martinez Moro, MdlA. . Ramirez, S. Moya, L. Salmon, J. Ruiz, D. Astruc, Dramatic synergy in CoPt Nanocatalysts Stabilized by "Click" dendrimers for evolution of hydrogen from hydrolysis of ammonia borane, ACS Catal. 9 (2019) 1110–1119, https://doi.org/10.1021/acscatal.8b04498.

[18] S. Zhou, Y. Yang, P. Yin, Z. Ren, L. Wang, M. Wei, Metal–support synergistic catalysis in Pt/MoO3–x nanorods toward ammonia borane hydrolysis with efficient hydrogen generation, ACS Appl. Mater. Interfaces , 14 (2022) 5275–5286, https://doi.org/10.1021/acsami.1c20736.

[19] S. Guan, L. An, S. Ashraf, L. Zhang, B. Liu, Y. Fan, B. Li, Oxygen vacancy excites Co3O4 nanocrystals embedded into carbon nitride for accelerated hydrogen generation, Appl. Catal. B 269 (2020) 118775, https://doi.org/10.1016/j.apcatb.2020.118775.

[20] J. He, Z. Yao, X. Xiao, W. Chen, Z. Huang, X. Fan, Z. Dong, X. Huang, X. Wang, M. Chen, L. Chen, Heterostructured Ni/NiO nanoparticles on 1D Porous MoOx for hydrolysis of ammonia borane, ACS Appl. Energy Mater. 4 (2021) 1208–1217, https://doi.org/10.1021/acsaem.0c02502.

[21] H. Lv, R. Wei, X. Guo, L. Sun, B. Liu, Synergistic catalysis of binary RuP nanoclusters on nitrogen-functionalized hollow mesoporous carbon in hydrogen production from the hydrolysis of ammonia borane, J. Phys. Chem. Lett. 12 (2021) 696–703, https://doi.org/10.1021/acs.jpclett.0c03547.

[22] P. Li, Y. Huang, Q. Huang, R. Chen, J. Li, S. Tian, Cobalt phosphide with porous multishelled hollow structure design realizing promoted ammonia borane dehydrogenation: elucidating roles of architectural and electronic effect, Appl. Catal. B (2022) 121444, https://doi.org/10.1016/j.apcatb.2022.121444.

[23] X. Yang, X. Ai, J.K. Yu, G.I.N. Waterhouse, L.Z. Sui, J. Ding, B.W. Zhang, X. Yong, S. Y. Lu, Photoluminescence mechanisms of red-emissive carbon dots derived from non-conjugated molecules, Sci. Bull. 67 (2022) 1450–1457, https://doi.org/10.1016/j.scib.2022.06.013.

[24] A.M. Al-Enizi, A. Nafady, M.M. El-Halwany, R.M. Brooks, A. Abutaleb, A. Yousef, Electrospun carbon nanofiber-encapsulated NiS nanoparticles as an efficient catalyst for hydrogen production from hydrolysis of sodium borohydride, Int. J. Hydrogen Energy 44 (2019) 21716–21725, https://doi.org/10.1016/j.ijhydene.2019.06.152.

[25] B. Wang, Z. Wei, L. Sui, J. Yu, B. Zhang, X. Wang, S. Feng, H. Song, X. Yong, Y. Tian, B. Yang, S. Lu, Electron–phonon coupling-assisted universal red

[26] J. Liu, P. Li, R. Jiang, X. Zheng, P. Liu, Ru nanoparticles immobilized on chitosan as effective catalysts for boosting NH3BH3 hydrolysis, ChemCatChem 13 (2021) 4142–4150, https://doi.org/10.1002/cctc.202100781.

[27] W. Chen, G. Lv, J. Fu, H. Ren, J. Shen, J. Cao, X. Liu, Demonstration of controlled hydrogen release using Rh@GQDs during hydrolysis of NH3BH3, ACS Appl. Mater. Interfaces 13 (2021) 50017–50026, https://doi.org/10.1021/acsami.1c15660.

[28] N. Wang, Q. Sun, T. Zhang, A. Mayoral, L. Li, X. Zhou, J. Xu, P. Zhang, J. Yu, Impregnating subnanometer metallic nanocatalysts into self-pillared zeolite nanosheets, J. Am. Chem. Soc. 143 (2021) 6905–6914, https://doi.org/10.1021/jacs.1c00578.

[29] Q. Xu, M. Chandra, Catalytic activities of non-noble metals for hydrogen generation from aqueous ammonia-borane at room temperature, J. Power Sources 163 (2006) 364–370, https://doi.org/10.1016/j.jpowsour.2006.09.043.

[30] K. Feng, J. Zhong, B. Zhao, H. Zhang, L. Xu, X. Sun, S.-T. Lee, CuxCo1−xO nanoparticles on graphene oxide as a synergistic catalyst for high-efficiency hydrolysis of ammonia–borane, Angew. Chem. Int. Ed. 55 (2016) 11950–11954, https://doi.org/10.1002/anie.201604021.

[31] Y. Ge, X. Qin, A. Li, Y. Deng, L. Lin, M. Zhang, Q. Yu, S. Li, M. Peng, Y. Xu, X. Zhao, M. Xu, W. Zhou, S. Yao, D. Ma, Maximizing the synergistic effect of CoNi catalyst on alpha-MoC for robust hydrogen production, J. Am. Chem. Soc. 143 (2021) 628–633, https://doi.org/10.1021/jacs.0c11285.

[32] H. Wu, S. Lu, B. Yang, Carbon-dot-enhanced electrocatalytic hydrogen evolution, Acc. Mater. Res. 3 (2022) 319–330, https://doi.org/10.1021/accountsmr.1c00194.

[33] C.-C. Hou, Q.-Q. Chen, K. Li, C.-J. Wang, C.-Y. Peng, R. Shi, Y. Chen, Tailoring three-dimensional porous cobalt phosphides templated from bimetallic metal–organic frameworks as precious metal-free catalysts towards the dehydrogenation of ammonia-borane, J. Mater. Chem. A 7 (2019) 8277–8283, https://doi.org/10.1039/C9TA00607A.

[34] W. Chen, J. Ji, X. Feng, X. Duan, G. Qian, P. Li, X. Zhou, D. Chen, W. Yuan, Mechanistic insight into size-dependent activity and durability in Pt/CNT catalyzed hydrolytic dehydrogenation of ammonia borane, J. Am. Chem. Soc. 136 (2014) 16736–16739, https://doi.org/10.1021/ja509778y.

[35] Q. Sun, X. Wang, H. Wang, H. Zhang, Q. He, Y. Zhang, Y. Cheng, X. Zhang, S. Shi, L. Tao, X. He, H. Ji, Crystal facet effects of platinum single-atom catalysts in hydrolytic dehydrogenation of ammonia borane, J. Mater. Chem. A 10 (2022) 10837–10843, https://doi.org/10.1039/d2ta01544g.

[36] C.-Y. Peng, L. Kang, S. Cao, Y. Chen, Z.-S. Lin, W.-F. Fu, Nanostructured Ni2P as a robust catalyst for the hydrolytic dehydrogenation of ammonia–borane, Angew. Chem. Int. Ed. 54 (2015) 15725–15729, https://doi.org/10.1002/anie.201508113.

[37] C.-C. Hou, Q. Li, C.-J. Wang, C.-Y. Peng, Q.-Q. Chen, H.-F. Ye, W.-F. Fu, C.-M. Che, N. Lopez, Y. Chen, Ternary Ni-Co-P nanoparticles as noble-metal-free catalysts to boost the hydrolytic dehydrogenation of ammonia-borane, Energy Environ. Sci. 10 (2017) 1770–1776, https://doi.org/10.1039/c7ee01553d.

[38] H. Zhang, Y. Liu, H. Wei, C. Wang, T. Liu, X. Wu, S. Ashraf, S. Mehdi, S. Guan, Y. Fan, X. Yue, B. Liu, Y. Zhang, H. Cao, B. Li, Atomic-bridge structure in B-Co-P dual-active sites on boron nitride nanosheets for catalytic hydrogen generation, Appl. Catal., B 314 (2022), 121495, https://doi.org/10.1016/j.apcatb.2022.121495.

[39] H. Zhang, K. Zhang, S. Ashraf, Y. Fan, S. Guan, X. Wu, Y. Liu, B. Liu, B. Li, Polar O–Co–P surface for bimolecular activation in catalytic hydrogen generation, Energy Environ. Mater. (2022), https://doi.org/10.1002/eem2.12273.

[40] H. Wu, Y. Cheng, B. Wang, Y. Wang, M. Wu, W. Li, B. Liu, S. Lu, Carbon dots-confined CoP-CoO nanoheterostructure with strong interfacial synergy triggered the robust hydrogen evolution from ammonia borane, J. Energy Chem. 57 (2021) 198–205, https://doi.org/10.1016/j.jechem.2020.08.051.

[41] J. Meng, C. Niu, L. Xu, J. Li, X. Liu, X. Wang, Y. Wu, X. Xu, W. Chen, Q. Li, Z. Zhu, D. Zhao, L. Mai, General oriented formation of carbon nanotubes from metal–organic frameworks, J. Am. Chem. Soc. 139 (2017) 8212–8221, https://doi.org/10.1021/jacs.7b01942.

[42] F. Xu, X. Liu, Magnetic Co-Pd/C nanocomposites for hydrogen evolution upon the hydrolytic dehydrogenation of NH3BH3, NaBH4, and Me2NHBH3, ACS Appl. Nano Mater. 4 (2021) 7479–7485, https://doi.org/10.1021/acsanm.1c01500.

[43] R. Shen, Y. Liu, H. Wen, X. Wu, G. Han, X. Yue, S. Mehdi, T. Liu, H. Cao, E. Liang, B. Li, Engineering bimodal oxygen vacancies and Pt to boost the activity toward water dissociation, Small 18 (2022), e2105588, https://doi.org/10.1002/smll.202105588.

[44] Y. Pan, K. Sun, Y. Lin, X. Cao, Y. Cheng, S. Liu, L. Zeng, W.-C. Cheong, D. Zhao, K. Wu, Z. Liu, Y. Liu, D. Wang, Q. Peng, C. Chen, Y. Li, Electronic structure and d-band center control engineering over M-doped CoP (M = Ni, Mn, Fe) hollow polyhedron frames for boosting hydrogen production, Nano Energy 56 (2019) 411–419, https://doi.org/10.1016/j.nanoen.2018.11.034.

[45] Y. Chen, S. Ji, Y. Wang, J. Dong, W. Chen, Z. Li, R. Shen, L. Zheng, Z. Zhuang, D. Wang, Y. Li, Isolated single iron atoms anchored on N-doped porous carbon as an efficient electrocatalyst for the oxygen reduction reaction, Angew. Chem. Int. Ed. 56 (2017) 6937–6941, https://doi.org/10.1002/anie.201702473.

[46] C. Wang, Y. Ren, J. Zhao, S. Sun, X. Du, M. Wang, G. Ma, H. Yu, L. Li, X. Yu, X. Zhang, Z. Lu, X. Yang, Oxygen vacancy-attired dual-active-sites Cu/Cu0.76Co2.24O4 drives electron transfer for efficient ammonia borane dehydrogenation, Appl. Catal., B 314 (2022), 121494, https://doi.org/10.1016/j.apcatb.2022.121494.

[47] M. Paladini, G.M. Arzac, V. Godinho, D. Hufschmidt, M.C.J. de Haro, A.M. Beltrán, A. Fernández, The role of cobalt hydroxide in deactivation of thin film Co-based

catalysts for sodium borohydride hydrolysis, Appl. Catal. B 210 (2017) 342–351, https://doi.org/10.1016/j.apcatb.2017.04.005.

[48] I. Platzman, R. Brener, H. Haick, R. Tannenbaum, Oxidation of polycrystalline copper thin films at ambient conditions, J. Phys. Chem. C 112 (2008) 1101–1108, https://doi.org/10.1021/jp076981k.

[49] J. Ghijsen, L.H. Tjeng, J. van Elp, H. Eskes, J. Westerink, G.A. Sawatzky, M. T. Czyzyk, Electronic structure of Cu_2O and CuO, Phys. Rev. B 38 (1988) 11322–11330, https://doi.org/10.1103/physrevb.38.11322.

[50] F. Shi, K. Huang, Y. Wang, W. Zhang, L. Li, X. Wang, S. Feng, Black phosphorus-modified Co_3O_4 through tuning the electronic structure for enhanced oxygen evolution reaction, ACS Appl. Mater. Interfaces 11 (2019) 17459–17466, https://doi.org/10.1021/acsami.9b04078.

[51] Z. Xiao, Y. Wang, Y.-C. Huang, Z. Wei, C.-L. Dong, J. Ma, S. Shen, Y. Li, S. Wang, Filling the oxygen vacancies in Co_3O_4 with phosphorus: an ultra-efficient electrocatalyst for overall water splitting, Energy Environ. Sci. 10 (2017) 2563–2569, https://doi.org/10.1039/C7EE01917C.

[52] P. Li, R. Chen, Y. Huang, W. Li, S. Zhao, S. Tian, Activating transition metal via synergistic anomalous phase and doping engineering towards enhanced dehydrogenation of ammonia borane, Appl. Catal. B 300 (2022), 120725, https://doi.org/10.1016/j.apcatb.2021.120725.

[53] L. Zhang, J. Ye, Y. Tu, Q. Wang, H. Pan, L. Wu, X. Zheng, J. Zhu, Oxygen modified CoP_2 supported palladium nanoparticles as highly efficient catalyst for hydrolysis of ammonia borane, Nano Res. 15 (2021) 3034–3041, https://doi.org/10.1007/s12274-021-3941-7.

[54] J. Yang, W. Fu, C. Chen, W. Chen, W. Huang, R. Yang, Q. Kong, B. Zhang, J. Zhao, C. Chen, J. Luo, F. Yang, X. Duan, Z. Jiang, Y. Qin, Atomic design and fine-tuning of subnanometric Pt catalysts to tame hydrogen generation, ACS Catal. 11 (2021) 4146–4156, https://doi.org/10.1021/acscatal.0c04614.